ASME Journal of Applied Mechanics
Online journal at:
https://asmedigitalcollection.asme.org/appliedmechanics

Zhi Zhao
Department of Civil and Environmental Engineering,
University of Illinois at Urbana-Champaign,
Urbana, IL 61801
e-mail: zhi4@illinois.edu

Chao Wang
Department of Civil and Environmental Engineering,
University of Illinois at Urbana-Champaign,
Urbana, IL 61801
e-mail: chaow4@illinois.edu

Xiaojia Shelly Zhang[1]
Assistant Professor
Department of Civil and Environmental Engineering,
University of Illinois at Urbana-Champaign,
Urbana, IL 61801;
Department of Mechanical Science and Engineering,
National Center for Supercomputing Applications,
University of Illinois at Urbana-Champaign,
Urbana, IL 61801
e-mail: zhangxs@illinois.edu

Tuning Buckling Behaviors in Magnetically Active Structures: Topology Optimization and Experimental Validation

Buckling, a phenomenon historically considered undesirable, has recently been harnessed to enable innovative functionalities in materials and structures. While approaches to achieve specific buckling behaviors are widely studied, tuning these behaviors in fabricated structures without altering their geometry remains a major challenge. Here, we introduce an inverse design approach to tune buckling behavior in magnetically active structures through the variation of applied magnetic stimuli. Our proposed magneto-mechanical topology optimization formulation not only generates the geometry and magnetization distribution of these structures but also informs how the external magnetic fields should be applied to control their buckling behaviors. By utilizing the proposed strategy, we discover magnetically active structures showcasing a broad spectrum of tunable buckling mechanisms, including programmable peak forces and buckling displacements, as well as controllable mechano- and magneto-induced bistability. Furthermore, we experimentally demonstrate that multiple unit designs can be assembled into architectures, resulting in tunable multistability and programmable buckling sequences under distinct applied magnetic fields. By employing a hybrid fabrication method, we manufacture and experimentally validate the generated designs and architectures, confirming their ability to exhibit precisely programmed and tunable buckling behaviors. This research contributes to the advancement of multifunctional materials and structures that harness buckling phenomena, unlocking transformative potential for various applications, including robotics, energy harvesting, and deployable and reconfigurable devices. [DOI: 10.1115/1.4062536]

Keywords: tunable magneto-mechanical buckling, programmable multistability, magnetic soft materials, topology optimization, experimental validation

1 Introduction

Buckling has long been studied as a fundamental mechanical instability that can cause the failure of slender structural components under compressive loads. However, recent advances in design and manufacturing techniques have transformed buckling into an opportunity to enable advanced functionalities rather than a limitation [1,2]. One particularly promising area of research is to design and control the buckling behavior of structures under external stimuli [3–5], such as mechanical load, temperature, electrical, or magnetic fields. By harnessing the buckling behavior of structures, engineers can create complex, adaptive, and multifunctional structures with applications including robotics [6], energy absorber [7], actuator [8], and assembly mechanisms [9].

Traditionally, the buckling behavior of structures remains fixed once fabricated, and modifying or tuning these behaviors without altering the geometry poses a major challenge. One approach to enable the tuning of buckling behaviors without geometric alterations involves leveraging multiphysics interactions between various stimuli, allowing one stimulus to act as a switch for guiding and tuning the structure's buckling response under another stimulus. In this study, we investigate the magneto-mechanical interaction in magnetically active structures and study the use of magnetic stimuli to control the buckling and stability of such structures due to the attractive features of magnetic stimuli, such as rapid, untethered, and wireless actuation [10]. Hard-magnetic soft materials, which embed high-coercivity hard-magnetic particles into a soft matrix [11,12], provide exceptional programmability and flexible control through the design of both structural geometry and premagnetization distribution. Previous research has employed hard-magnetic soft materials to design and develop magneto-mechanical metamaterials and structures with programmable mechano-induced buckling, which can be tuned by applying magnetic fields [13–16]. However, these studies have predominantly relied on intuition-driven design methods, potentially restricting their capability to thoroughly explore the entire design space. A systematic design approach that encompasses the full design space could significantly enhance the programmability of tunable buckling behaviors.

[1]Corresponding author.

Manuscript received April 21, 2023; final manuscript received May 9, 2023; published online June 9, 2023. Tech. Editor: Pradeep Sharma.

Topology optimization, an optimization-driven design approach, has gained considerable interest in recent years due to its capacity to generate freeform designs by comprehensively exploring the design space given specific design requirements and constraints [17,18]. Structural topology optimization formulations have been developed for the inverse design of structures with programmable buckling behaviors under purely mechanical loads [19–21]. Recent work establishes topology optimization approaches for hard-magnetic soft materials, primarily focusing on programming deformation and actuation of these magnetically active structures under magnetic fields [22–25]. However, topology optimization approaches for the inverse design of hard-magnetic soft materials to enable tunable magneto-mechanical buckling responses remain unexplored.

This study proposes and validates a magneto-mechanical topology optimization framework for the inverse design of structures made from hard-magnetic soft materials. The goal is to achieve tunable buckling responses by harnessing nonlinear magneto-mechanical interactions. The framework simultaneously optimizes the geometry and magnetization distribution of the structures, as well as the control strategies for the applied magnetic fields. As depicted in Fig. 1, the versatile inverse design framework enables the creation of designs that exhibit tunable buckling behaviors in response to either magneto-mechanical or purely magnetic stimuli. Under magneto-mechanical stimuli, the framework discovers designs whose mechano-induced buckling behaviors, such as peak forces and buckling displacements, can be controlled by varying applied magnetic fields. Under purely magnetic stimuli, the framework generates designs whose magneto-induced buckling behaviors can be programed to realize either self-recovering or self-locking deformations. By assembling multiple optimized designs, we further create architectures that display tunable multistability and programmable buckling sequences under distinct applied magnetic fields. We also investigate the underlying mechanisms and multiphysics interactions, which result in the tunable magneto-mechanical buckling responses. By employing a hybrid fabrication procedure, we manufacture optimized structures and architectures and conduct experimental tests to validate their programmed buckling behaviors. The experimental results show excellent agreements with numerical predictions across all cases.

This article is organized as follows: Sec. 2 introduces the constitutive model and finite element analysis (FEA) for hard-magnetic soft materials. Section 3 briefly summarizes the parameterization and interpolation schemes and presents the proposed optimization formulation. Section 4 presents the protocol for fabricating optimized designs. Section 5 presents the numerical investigations and experimental validations for the magneto-tunable and mechano-induced buckling designs. Section 6 discusses the magneto-induced buckling designs that possess self-recovery and self-locking features. Finally, this article concludes with several remarks in Sec. 7. Appendix presents the material characterization protocol. Supplementary Videos 1–5 show the experimental validation and demonstration of the generated designs exhibiting tunable magneto-mechanical buckling behaviors.

2 Constitutive Model and Nonlinear Finite Element Analysis for Hard-Magnetic Soft Materials

This section provides a concise overview of the constitutive model that describes the magneto-mechanical behavior of hard-magnetic soft materials under finite deformations. It is followed by a discussion of the corresponding FEA, which employs a total Lagrangian framework.

Consider a deformable solid occupying a domain Ω in its undeformed state, where $\mathbf{X}$ represents the position vector. The solid is subjected to an applied displacement field $\tilde{\mathbf{u}}$ on the boundary Γ_u and an applied traction on Γ_t, such that $\Gamma_u \cup \Gamma_t$ constitutes the boundary $\partial\Omega$, and $\Gamma_u \cap \Gamma_t = \varnothing$. The deformation of the solid is described by a deformation map χ, which maps a material point $\mathbf{X}$ to its corresponding position $\mathbf{x} = \chi(\mathbf{X})$. The deformation gradient tensor $\mathbf{F}$ is defined as $\mathbf{F} = \nabla\chi$, where ∇ denotes the gradient operator with respect to the undeformed configuration.

This study adopts a constitutive model for ideal hard-magnetic soft materials developed in [11], which has been validated to possess prediction in great agreement with experimental results [10,11]. We denote $\mathbf{B}_r$ and $\mathbf{B}_a$ as residual magnetic flux density for hard-magnetic soft material and externally applied magnetic flux density in the undeformed configuration, respectively. To construct the constitutive model for hard-magnetic soft materials,

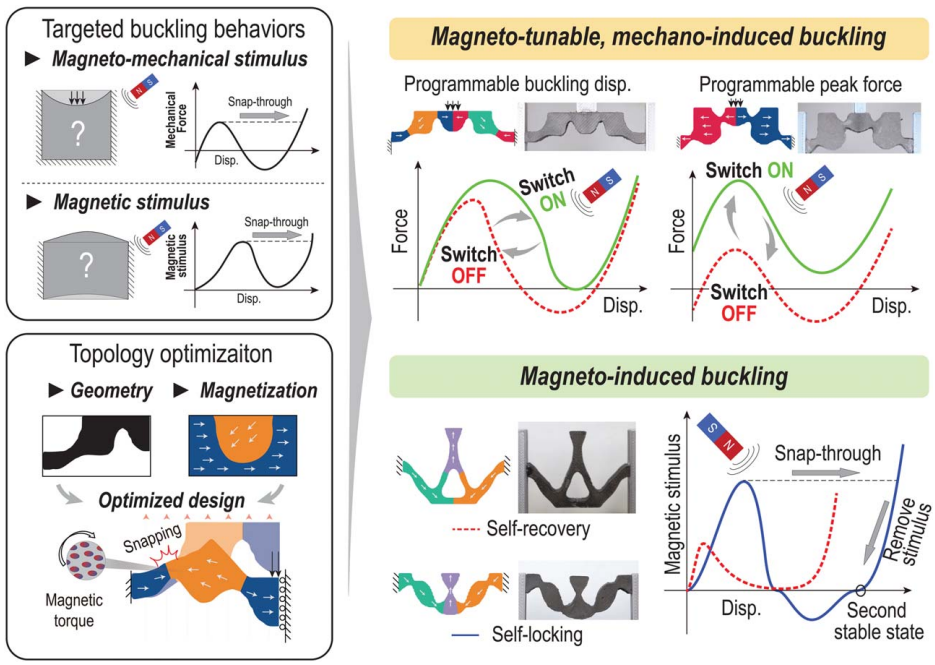

Fig. 1 The proposed multiphysics topology optimization framework to enable tunable magneto-mechanical buckling behaviors

several rational assumptions are introduced to simplify what would otherwise be a complex and coupled nonlinear magneto-mechanical theory. These assumptions include [11]: (1) The magnetic material is magnetically saturated and retains a residual magnetic flux density $\mathbf{B}_r$ independent of the external magnetic field $\mathbf{H}$, whose strength is much lower than the magnetic coercivity $\mathbf{H}_c$. (2) The magnetic permeability μ of premagnetized hard-magnetic soft material is assumed to be the vacuum (or air) permeability, i.e., $\mu = \mu_0 = 1.257 \times 10^{-6}$ H/m. (3) In this study, the applied magnetic flux density $\mathbf{B}_a$ is assumed to be a uniform vector. We recognize that the model may have limitations under significant stretching [26] or large applied magnetic fields [27]. However, due to its simplicity, it is advantageous and necessary for establishing an optimization approach, which usually involves hundreds of magneto-mechanical simulations to obtain a well-defined design.

According to the theory, the constitutive relation of the ideal hard-magnetic soft materials is described by the following nominal Helmholtz free energy function (per unit volume in the undeformed configuration):

$$W(\mathbf{F}) = W_E(\mathbf{F}) + W_M(\mathbf{F}) = W_E(\mathbf{F}) - \frac{1}{\mu_0}\mathbf{F}\mathbf{B}_r \cdot \mathbf{B}_a \tag{1}$$

where $W_M(\mathbf{F})$ is magnetic free energy and $W_E(\mathbf{F})$ is the hyperelastic stored energy for soft matrix materials (e.g., elastomers) with magnetic particles.

In order to accurately describe the mechanical behavior of the two-phase composite material consisting of matrix materials and rigid particles (assuming magnetic particles are rigid), we utilize an isotropic and incompressible hyperelastic stored energy model of filled elastomers [28]. The model can be expressed as follows:

$$W_E(\mathbf{F}) = (1-c)\psi(\tilde{I}_1) \quad \text{with} \quad \tilde{I}_1 = \frac{I_1 - 3}{(1-c)^{7/2}} + 3 \tag{2}$$

where c represents the volume ratio for magnetic particles and I_1 is the first principal invariant of the right Cauchy–Green deformation tensor $\mathbf{C} = \mathbf{F}^T\mathbf{F}$. The function $\psi(\cdot)$ is defined by the expression given in [29]:

$$\psi(\tilde{I}_1) = \sum_{i=1}^{N_L} \frac{3^{1-\alpha_i}}{2\alpha_i}\mu_i(\tilde{I}_1^{\alpha_i} - 3^{\alpha_i}) \tag{3}$$

where α_i ($i = 1, 2, \ldots, N_L$) are real-valued constants and $\mu = \sum_{i=1}^{N_L}\mu_i$ is the second Lamé parameter under the initial state. In this study, we consider two sets of terms in the hyperelastic stored energy function, i.e., $N_L = 2$.

In the undeformed configuration, the equilibrium of the solid is governed by the following partial differential equations with body force neglected:

$$\begin{aligned} &\nabla \cdot \mathbf{P} = \mathbf{0} \quad \text{in } \Omega, \\ &\mathbf{u} = \tilde{\mathbf{u}} \quad \text{on } \Gamma_u, \\ &\mathbf{P}\mathbf{N} = \tilde{\mathbf{t}} \quad \text{on } \Gamma_t \end{aligned} \tag{4}$$

where $\mathbf{P}$ is the first Piola–Kirchhoff stress, $\nabla\cdot$ stands for the divergence operator in the undeformed configuration, $\mathbf{N}$ is the outward unit vector normal to the undeformed boundary of the solid, and $\tilde{\mathbf{t}}$ is the applied traction.

On the basis of the finite element theory [30], we construct a finite element mesh Ω_h consisting of N_e elements and N_n nodes. We can express the total potential energy $\Pi(\mathbf{u})$ and its stationary condition $\mathbf{r}(\mathbf{u})$ as follows:

$$\Pi(\mathbf{u}) = \sum_{e=1}^{N_e}\int_{\Omega_e} W(\mathbf{u}_e)d\mathbf{X} - (\mathbf{f}_{ext})^T\mathbf{u} \tag{5}$$

$$\mathbf{r}(\mathbf{u}) = \frac{\partial \Pi}{\partial \mathbf{u}}(\mathbf{u}) = \mathbf{f}_{int}(\mathbf{u}) - \mathbf{f}_{ext}(\mathbf{u}) = \mathbf{0} \tag{6}$$

respectively, where Ω_e is the elementwise mesh domain, $\mathbf{u}$ represents the displacement vector, $\mathbf{r}$ is the global residual vector, $\mathbf{f}_{int}$ is the internal force vector, and $\mathbf{f}_{ext}$ is the external force vector. To solve the nonlinear system of equations, the Newton–Raphson procedure [30] with an inexact line search method [31,32] is used iteratively. This study employs displacement-based finite elements in 2D under the plane stress condition, which ensures that volumetric locking does not occur even for soft materials with incompressible behaviors.

3 Topology Optimization Framework for Designs With Tunable Magneto-Mechanical Buckling Behavior

In this section, a brief summary of the design space parameterization and interpolation schemes proposed in Ref. [22] is provided for completeness. The section then presents a topology optimization formulation that utilizes the established design parametrization and interpolation schemes to generate structural designs with tunable magneto-mechanical buckling behaviors.

3.1 Parameterization of Geometry. We utilize a density-based approach [17] to associate the geometry to a physical design variable $\overline{\rho}_e$ for each element, where $\overline{\rho}_e$ indicates whether a location in space is solid ($\overline{\rho}_e = 1$) or void ($\overline{\rho}_e = 0$). The physical density variables $\overline{\boldsymbol{\rho}}$ are obtained using a Heaviside projection operator with a threshold of 1/2 [33]:

$$\overline{\rho}_e = \frac{\tanh(\beta_\rho/2) + \tanh(\beta_\rho(\widetilde{\rho}_e - (1/2)))}{2\tanh(\beta_\rho/2)} \tag{7}$$

where β_ρ controls the discreteness of the projection. The intermediate variable $\widetilde{\rho}_e$ is regularized using the density filter [34] according to the following equation:

$$\widetilde{\rho}_e = \frac{\sum_{i\in\mathcal{I}_e(R_\rho)} w_\rho^{(i,e)} v_i \rho_i}{\sum_{i\in\mathcal{I}_e(R_\rho)} w_\rho^{(i,e)} v_i} \tag{8}$$

where the set $\mathcal{I}_e(R_\rho)$ represents the eth element set within a region defined by a circle centered at the centroid of the eth element with a radius of R_ρ, v_i is the volume of the ith element, and the weighting factor $w_\rho^{(i,e)}(R_\rho)$ is determined by the distance between the centroids of the ith and eth elements (denoted as $\mathbf{X}_i$ and $\mathbf{X}_e$, respectively), which is given by $w_\rho^{(i,e)} = 1 - (|\mathbf{X}_i - \mathbf{X}_e|/R_\rho)$.

3.2 Parameterization of Magnetization Distribution. The residual magnetic flux density in each location of the design is chosen from a predetermined set of N_m candidate residual magnetic flux densities, denoted as $\mathbf{B}_r^{(1)},\ldots,\mathbf{B}_r^{(N_m)}$, each pointing in a specific direction. The residual magnetic flux density in element e is expressed as follows:

$$\mathbf{B}_{r,e} = \sum_{j=1}^{N_m}\left(\overline{m}_e^{(j)}\right)^{p_m}\mathbf{B}_r^{(j)} \tag{9}$$

In the aforementioned interpolation, $\overline{m}_e^{(j)}$ represents the physical magnetization variable, which indicates the magnetization of element e: $\overline{m}_e^{(j)} = 1$ means that the jth candidate residual magnetic flux density $\mathbf{B}_r^{(j)}$ is selected, while $\overline{m}_e^{(j)} = 0$ indicates that the jth candidate residual magnetic flux density $\mathbf{B}_r^{(j)}$ is not selected. To penalize the mixture of candidate magnetizations, we introduce a solid isotropic material with penalization (SIMP)-type [17,35] penalization power p_m.

To further promote discrete magnetization distribution and accommodate nonmagnetized regions in our designs, we adopt the hypercube-to-simplex projection (HSP) approach [36]. The HSP approach has demonstrated robust performance based on our

experience [22], and its expression is as follows:

$$\overline{m}_e^{(j)} = \sum_{i=1}^{2^{N_m}} s_i^{(j)} \left((-1)^{\left(N_m + \sum_{k=1}^{N_m} c_i^{(k)}\right)} \prod_{k=1}^{N_m} \left(\overline{\xi}_e^{(k)} + c_i^{(k)} - 1 \right) \right) \tag{10}$$

where $\overline{\xi}_e^{(j)}$ is the intermediate variable obtained from similar filtering and projection operations through the same expressions in Eqs. (7) and (8). The parameter $c_i^{(j)} = \{0, 1\}$ is the ith vertex of a N_m-dimensional unit hypercube for the jth candidate remnant magnetization vector and $s_i^{(j)}$ is the mapped vertex of a N_m-dimensional standard simplex domain:

$$s_i^{(j)} = \begin{cases} \dfrac{c_i^{(j)}}{\sum_{k=1}^{N_m} c_i^{(k)}} & \text{if } \sum_{k=1}^{N_m} c_i^{(k)} \geq 1, \\ 0 & \text{otherwise} \end{cases} \tag{11}$$

3.3 Interpolation of the Helmholtz Free Energy Function. To characterize the nonlinear magneto-mechanical properties of hard-magnetic soft materials, we apply an interpolation method to the Helmholtz free energy function based on physical variables $\overline{\boldsymbol{\rho}}$ and $\overline{\mathbf{m}}^{(j)}$, $j = 1, \ldots, N_m$. The interpolated free energy W_I of element e under stimulus ℓ is given by

$$W_I\left(\overline{\rho}_e, \overline{m}_e^{(1)}, \ldots, \overline{m}_e^{(N_m)}, \mathbf{u}_e^{(\ell)}\right) = \left(\varepsilon + (1-\varepsilon)(\overline{\rho}_e)^{p_\rho}\right) W_E\left(\mathbf{u}_e^{(\ell)}\right) + (\overline{\rho}_e)^{p_\rho} W_M\left(\mathbf{u}_e^{(\ell)}, \mathbf{B}_{r,e}(\overline{m}_e^{(1)}, \ldots, \overline{m}_e^{(N_m)})\right) \tag{12}$$

where $\mathbf{u}_e^{(\ell)}$ is the displacement vector in element e under stimulus ℓ and we introduce a small value of $\varepsilon = 10^{-5}$ to avoid numerical singularity. To penalize both hyperelastic stored energy and magnetic free energy and promote a nearly discrete design, we use the SIMP approach [17,35] in the aforementioned interpolation formula, driving the variable $\overline{\rho}_e$ toward either 0 or 1. To alleviate excessive deformations of low-density regions that can lead to numerical instabilities in FEA during optimization, we employ an energy interpolation scheme [37] for both the stored energy W_E and magnetic energy W_M.

3.4 Proposed Optimization Formulation. By using the design space parameterization and free energy interpolation schemes, we present a topology optimization formulation for generating designs with magneto-mechanical buckling behaviors. Formally, we formulate the topology optimization problem as follows:

$$\begin{aligned} \min_{\boldsymbol{\rho}, \boldsymbol{\xi}^{(1)}, \ldots, \boldsymbol{\xi}^{(N_m)}} \; & J\left(\mathbf{u}^{(\ell)}\right) = \max\left(F(\mathbf{u}^{(\ell)})\right), \quad \ell \in 1, \ldots, N_\ell, \\ \text{s.t.:} \quad & F(\mathbf{u}^{(\ell)}) \geq F_{\min}^{(\ell)}, \quad \ell \in 1, \ldots, N_\ell, \\ & D(\mathbf{u}^{(\ell)}) \geq D_{\min}^{(\ell)}, \quad \ell \in 1, \ldots, N_\ell, \\ & \frac{\mathbf{v}^T \overline{\boldsymbol{\rho}}}{|\Omega_h|} \leq v_{\max}, \\ & \left\{ \sum_{e=1}^{N_e} \left[\frac{w_\sigma(\overline{\rho}_e)}{v_e} \int_{\Omega_{h,e}} \sigma_{VM}\left(\boldsymbol{\sigma}_E\left(\mathbf{u}^{(\ell)}\right)\right) d\mathbf{X} \right]^{p_n} \right\}^{1/p_n} \\ & \quad \leq \sigma_{\max}^{(\ell)}, \quad \ell = 1, \ldots, N_\ell, \\ & \mathbf{r}(\overline{\boldsymbol{\rho}}, \overline{\mathbf{m}}^{(1)}, \ldots, \overline{\mathbf{m}}^{(N_m)}, \mathbf{u}^{(\ell)}) = \mathbf{0}, \quad \ell = 1, \ldots, N_\ell, \\ & \mathbf{0} \leq \boldsymbol{\rho} \leq \mathbf{1}, \\ & \mathbf{0} \leq \boldsymbol{\xi}^{(j)} \leq \mathbf{1}, \quad j = 1, \ldots, N_m \end{aligned} \tag{13}$$

where the converged displacement vector obtained under stimulus ℓ is denoted by $\mathbf{u}^{(\ell)}$. The objective function evaluated at $\mathbf{u}^{(\ell)}$ is given by $J(\mathbf{u}^{(\ell)}) = F(\mathbf{u}^{(\ell)})$, where the force F is the summation of internal forces at the target degree-of-freedom. Force constraints are utilized to ensure that the force F exceeds a predetermined lower bound, denoted by $F_{\min}^{(\ell)}$. In order to induce snap-through buckling behaviors [20,38], the objective is typically applied at a higher displacement level, while the minimal force constraint is enforced at a lower displacement level, as illustrated in Fig. 2(*a*). By adjusting the two displacement levels and $F_{\min}^{(\ell)}$ under various types of magneto-mechanical stimuli, the designs can be configured to exhibit magneto-tunable and mechano-induced buckling behaviors, with programmable buckling displacements or peak forces.

The optimization mechanism described earlier can be used to enable designs with magneto-induced buckling by introducing a displacement constraint that is solely applied under the magnetic stimulus. Figure 2(*b*) illustrates this approach. If a mechano-induced snap-through buckling design, enabled through a force objective

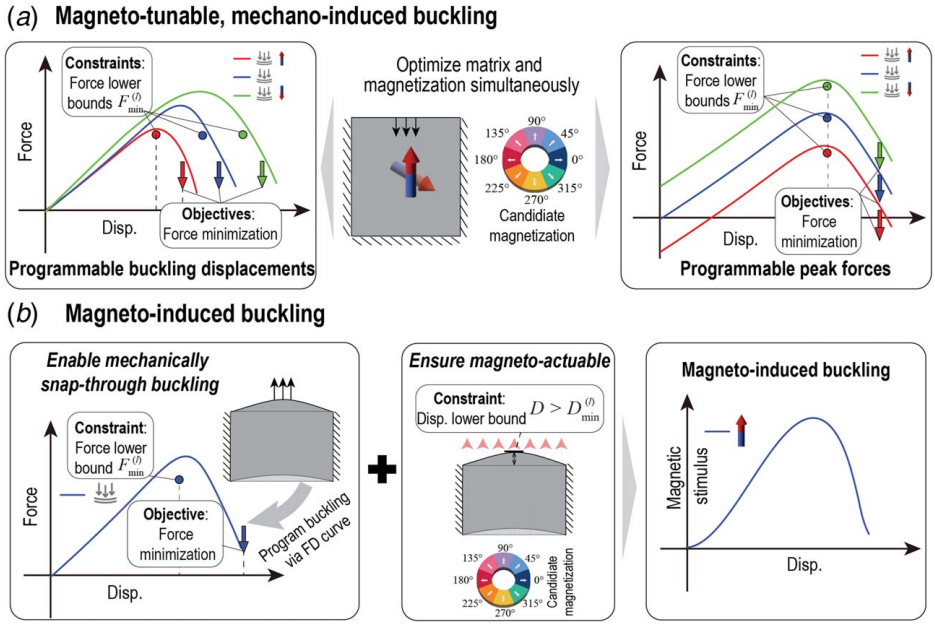

Fig. 2 Proposed optimization formulations for designing structures that display buckling behaviors (*a*) induced by mechanical loads, tunable by magnetic fields, or (*b*) induced by purely magnetic fields

and constraints described earlier, can also be actuated under a magnetic field to achieve sufficient displacement, it could exhibit snap-through behavior under the pure magnetic stimulus. It is important to note that this optimization setup indirectly controls magneto-induced buckling behaviors, and our future work will involve direct control, such as programing the relationship between magnetic stimulus and displacement.

The proposed optimization formulation includes a volume usage constraint, with $\mathbf{v}$ representing the element volume vector and $v_{\max}$ being the upper bound of the volume ratio assigned for matrix materials. Stress constraints [22,39] are also incorporated to ensure that the maximum von Mises stress associated with the mechanical Cauchy stress tensor $\boldsymbol{\sigma}_{\mathrm{E}} = 1/J(\partial W_{\mathrm{E}}(\mathbf{F})/\partial \mathbf{F})\mathbf{F}^{\mathrm{T}}$ does not exceed a predetermined upper limit $\sigma_{\max}^{(\ell)}$. To avoid singularity issues in stress-constrained topology optimization [39,40], a relaxation approach is utilized. In this approach, a function $w_\sigma(\overline{\rho}_e) = \varepsilon + (1-\varepsilon)\overline{\rho}_e^{q_\rho}$ is defined, where $q_\rho < 1$. The maximum stress is estimated using the p-norm approach [39] with the power of p_{n}. It is worth noting that stress constraints serve as a numerical technique to prevent the optimized design from containing thin members and hinge-like connections and to limit the level of local deformations [22]. Additionally, the equilibriums for stimuli ℓ are nested constraints within the formulation.

We use a gradient-based update algorithm, specifically the method of moving asymptotes [41], to solve the proposed formulation (13). The sensitivities of objective and constraint functions with respect to the design variables are obtained through the adjoint method [22,25].

4 Fabrication Approach for Topology-Optimized Magnetically Active Designs

In this section, we describe the process for fabricating designs that consist of hard-magnetic and soft materials. The overall fabrication procedures are illustrated in Fig. 3. Dow Sylgard 184 Kit (polydimethylsiloxane (PDMS)) (Fisher Scientific) and NdFeB particles with an average particle size of 25 μm (Magnequench) are used to fabricate hard-magnetic soft materials. First, the base, agent, and NdFeB particles are mixed for 20 min in a tray and then degassed under a pressure of −0.8 atmosphere for 1 h to remove any trapped air bubbles. Next, the degassed mixture is injected into polyvinyl alcohol (PVA) molds with various geometries obtained from optimized designs (e.g., the one shown in Fig. 3(*a*)). These molds are printed using a fused deposition modeling (FDM) printer (Prusa Research). As illustrated in Fig. 3(*b*), the mixture and mold are then cured at 80 °C for 2 h in an oven before demolding. Notably, the PVA mold is soft and fragile at high temperatures, which greatly simplifies the demolding process. Based on the optimized magnetization directions, different parts are individually magnetized under a 2 T magnetizing field generated by an impulse magnetizer (IM-10-30, ASC Scientific) and placed into a complete sample mold. We bond different parts by injecting the uncured mixture onto the interfaces and curing at 80 °C for 2 h in an oven. Figure 3(*c*) displays the fabricated samples that are produced in the study.

5 Programing Magneto-Tunable and Mechano-Induced Buckling Behaviors

In this section, we perform inverse design to obtain structures whose mechano-induced buckling behaviors (i.e., buckling triggered by mechanical force), such as buckling displacements and peak forces, can be tuned by magnetic actuation. We present two optimized structures obtained from the formulation illustrated in Fig. 2(*a*), which realize programmable buckling displacements and peak forces, respectively. We compare the experimentally obtained force–displacement (FD) relations with those obtained from numerical simulations. Furthermore, we show that the second optimized structure exhibits distinct buckling peak forces under varying magnetic fields, allowing us to control self-recovering and self-locking buckling deformations in the structure by changing the magnetic field directions. Additionally, we demonstrate the ability to reprogram the buckling sequence in an architecture assembled from this structure using different magnetic fields. We experimentally demonstrate these two interesting behaviors. Note that the material used for the designs discussed in this section is a mixture of PDMS with a base-to-agent ratio of 20:1 and magnetic particles with a volume ratio of 15%. The material properties are characterized according to the protocol described in the Appendix. To ensure a fair comparison between experimental results and numerical simulations, we use body-fitted meshes for simulation. This approach ensures that the mesh conforms to the exact geometry of the fabricated samples, which have complex and nonuniform shapes.

To experimentally validate our designs, we conduct tests to measure the FD relations under magnetic fields. To accomplish this, we utilize the experimental setup illustrated in Fig. 4. The loading bars, frames, and supports are 3D printed using polylactic

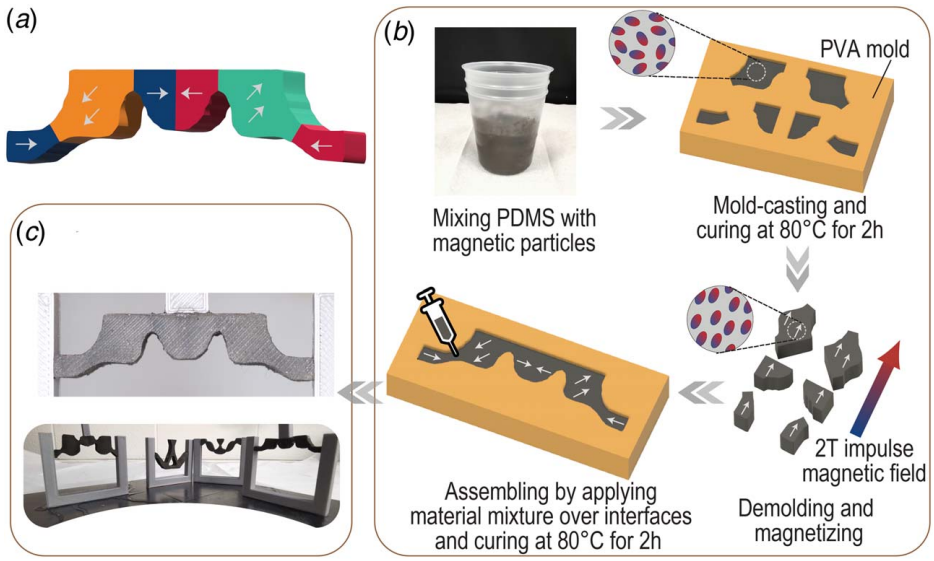

Fig. 3 Fabrication process for the hard-magnetic soft material: (*a*) optimized design, (*b*) mold casting, magnetization, and bonding, and (*c*) fabricated samples

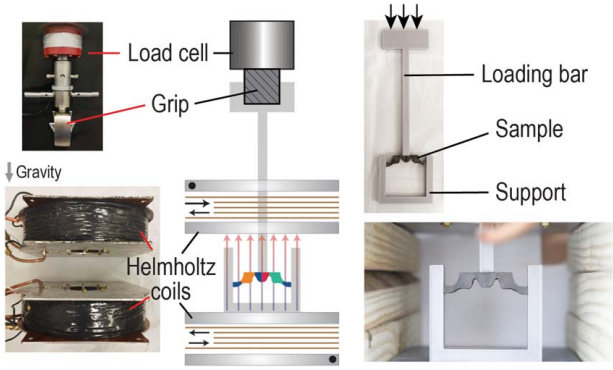

Fig. 4 Experiment setup to test force–displacement relations of magneto-tunable and mechano-induced buckling designs

acid (PLA) with an FDM printer. The specimens are attached to the PLA prints using superglue according to the corresponding boundary conditions. A uniform magnetic field is generated using a pair of Helmholtz coils (Woodruff Scientific) and measured using a Gauss meter (PCE-MFM 4000). To position the specimen between the Helmholtz coils and apply a load using a loading machine (Instron 68TM-30), wood blocks are used to fill in the gaps between the coils. A camera (SONY α7R) is positioned appropriately to record the experiment videos.

5.1 Programmable Buckling Displacements. We aim to optimize geometry and magnetization distributions to achieve designs with magneto-tunable and mechano-induced buckling displacements. The design domain is a 60 mm × 60 mm with three sides fixed, as shown in Fig. 5(*a*). We apply displacement loading to the middle top of the domain. To optimize the magnetization distribution, we consider $N_m = 8$ candidate magnetization vectors with a uniform orientation space of 45 deg and a magnitude of 100 mT. We apply three sets of stimuli with identical mechanical loads but varying magnetic fields: stimuli I, II, and III have an upward magnetic field ($B_a = 40$ mT), no magnetic field, and a downward magnetic field ($B_a = -40$ mT), respectively. To enable the design to have different buckling displacements under the three stimuli, we set three lower bounds (1 N) for the resultant force F evaluated at three displacement levels D of 5 mm, 10 mm, and 15 mm. We correspondingly minimize the resultant force at these displacement levels with a 5-mm offset (i.e., 10 mm, 15 mm, 20 mm), as illustrated in the left panel of Fig. 2(*a*). The volume upper bound is taken as 0.2.

An exemplary design with magneto-tunable buckling displacement is obtained and fabricated by a hybrid fabrication approach (see Sec. 4), as shown in Fig. 5(*b*). The FD relations obtained from numerical simulation and experiment are presented in Fig. 5(*c*). The structure undergoes snapping buckling triggered by a mechanical stimulus, with magnetic actuation acting as a "switch" that can either facilitate or hinder the structural buckling. This is observed in the boxed deformation configurations: for $D =$ 10 mm, the structure only buckles under stimuli I; for $D =$ 13 mm, the structure under stimuli II starts to buckle; and for $D = 16$ mm, the structure under all the stimuli cases buckles. To gain a deeper understanding of the snapping buckling phenomenon, we conduct numerical simulations using the arc-length method [42]. Our analysis reveals that the buckling observed in the structure

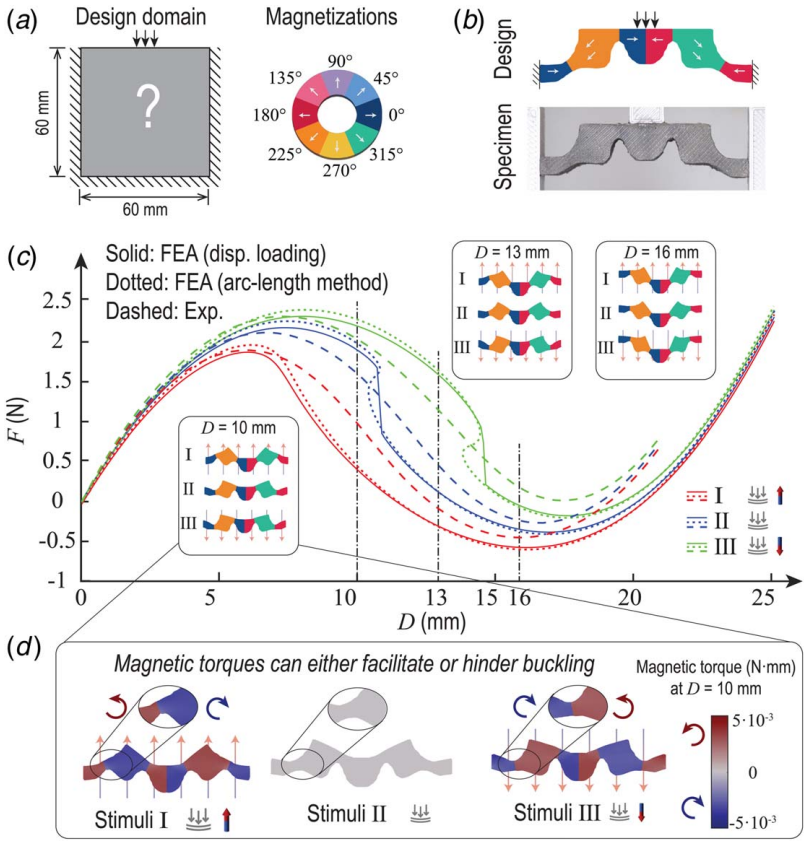

Fig. 5 An exemplary design of the magneto-tunable and mechano-induced buckling structure with programmable buckling displacements: (*a*) design domain and candidate magnetizations, (*b*) the optimized design and corresponding fabricated specimen, (c) force–displacement relations under three sets of stimuli (bottom curves: stimuli I, middle curves: stimuli II, top curves: stimuli III), and (*d*) magnetic torque contours at $D = 10$ mm under three sets of stimuli

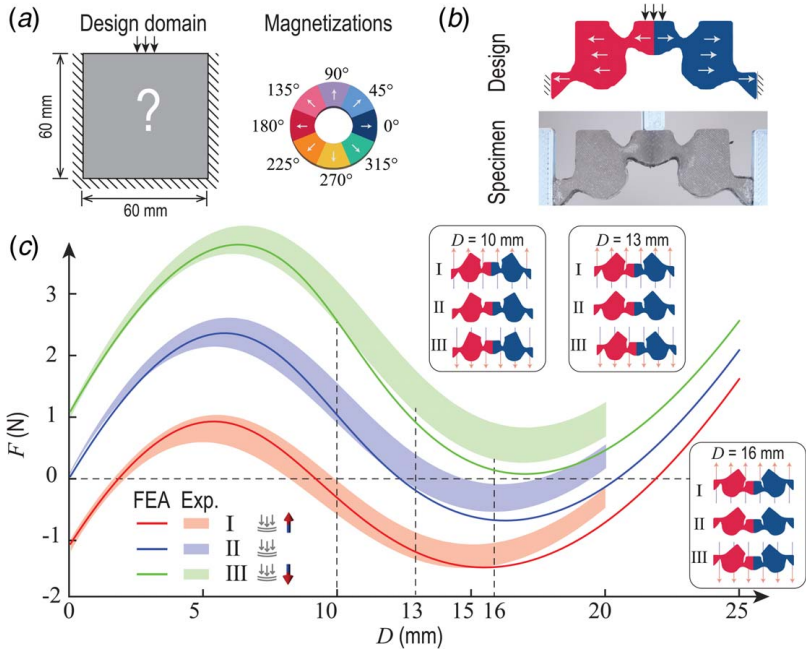

Fig. 6 An exemplar design of the magneto-tunable and mechano-induced buckling structure with programmable peak forces: (*a*) design domain and candidate magnetizations, (*b*) the optimized design and corresponding fabricated specimen, and (c) force–displacement relations under three sets of stimuli (bottom curve: stimuli I, middle curve: stimuli II, top curve: stimuli III). The shaded area represents the experimental results' mean value with their standard deviation added and subtracted.

under stimuli II and III exhibits a snap-back buckling behavior. In order to gain deeper insights into the mechanism of facilitated or hindered buckling by magnetic stimulus, we have plotted the magnetic torque contours [11] for the three sets of stimuli at $D = 10$ mm in Fig. 5(*d*). Our observations suggest that magnetic torques induced by magnetic actuation can facilitate or hinder buckling at critical member joints, corresponding to stimuli I or III, respectively.

Upon comparing the experimental and simulation results, we observe that they exhibit the same trend of buckling phenomenon with magneto-tunable buckling displacement. Regarding the experimental results, it is worth noting that the snap-back buckling behaviors could not be fully captured due to the limitations of the loading machine, which only allows displacement loading. Additionally, we acknowledge that testing this specific design is challenging to be fabricated due to the small post-bonded regions between the interfaces of different magnetization parts, which can initiate cracks and lead to fractures under large deformation. We conduct five replicate tests, and one of them does not result in

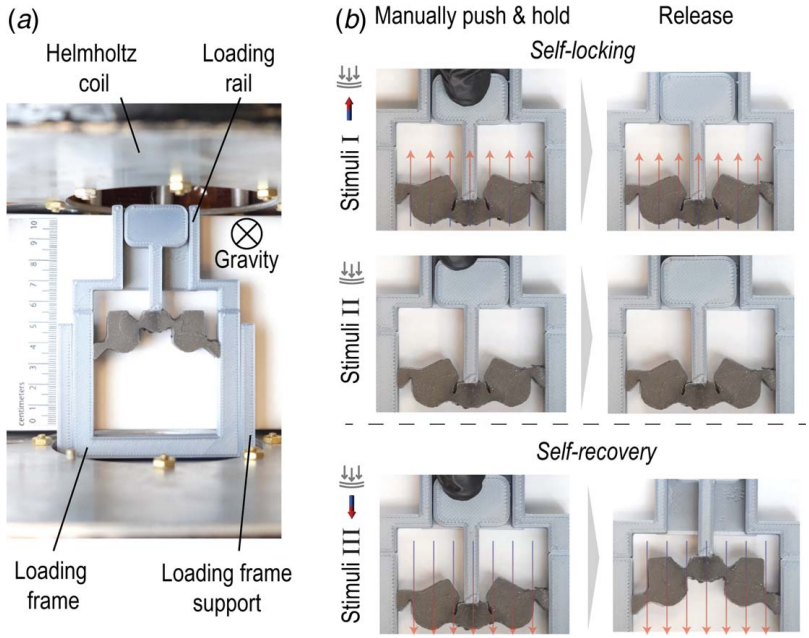

Fig. 7 Experimental demonstration for magneto-tunable self-recovery and self-locking behaviors: (*a*) experiment setup and (*b*) deformation configurations under different stimuli

fracturing, as depicted in Fig. 5(*c*). To address the issue of fracturing, an advanced fabrication approach, such as direct ink writing [43], can be utilized to eliminate postbonding. Mitigating this challenge is a critical area of focus for future research. Supplementary Video 1 provides documentation of the deformation history and FD relations obtained from both numerical simulation and experiment.

5.2 Programmable Peak Forces. Our aim in this section is to optimize the geometry and magnetization distribution to create designs that exhibit mechano-induced buckling with tunable peak forces, which can be controlled by magnetic stimuli. We conduct numerical and experimental investigations to analyze the tunable buckling behaviors. The magneto-tunable peak force feature of our designs enables flexible control of self-locking or self-recovery behaviors. Additionally, strategically assembling the optimized designs can lead to controllable sequential buckling behaviors under magnetic stimuli.

The design setup used in this section (shown in Fig. 6(*a*)) is the same as the one described in Sec. 5.1, with the exception of the specific details presented below. In order to achieve distinct peak forces for the design under stimuli I–III, we set different lower bounds (1 N, 2 N, and 3 N, respectively) for the resultant force F, evaluated at the displacement levels of 7.5 mm, and perform a minimization of F at a displacement level of 15 mm. The magnitude of applied magnetic flux density B_a is increased to 55 mT.

We present an exemplar design and the corresponding fabricated sample with magneto-tunable peak force levels, as shown in Fig. 6(*b*). The design exhibits snap-through behaviors upon mechanical load, stemming from its two-leg-like geometry under compressive mechanical load, as shown in Fig. 6(*c*). In the presence of magnetic stimuli, the internal magnetization aligns with the external magnetic fields, causing additional responsive forces and

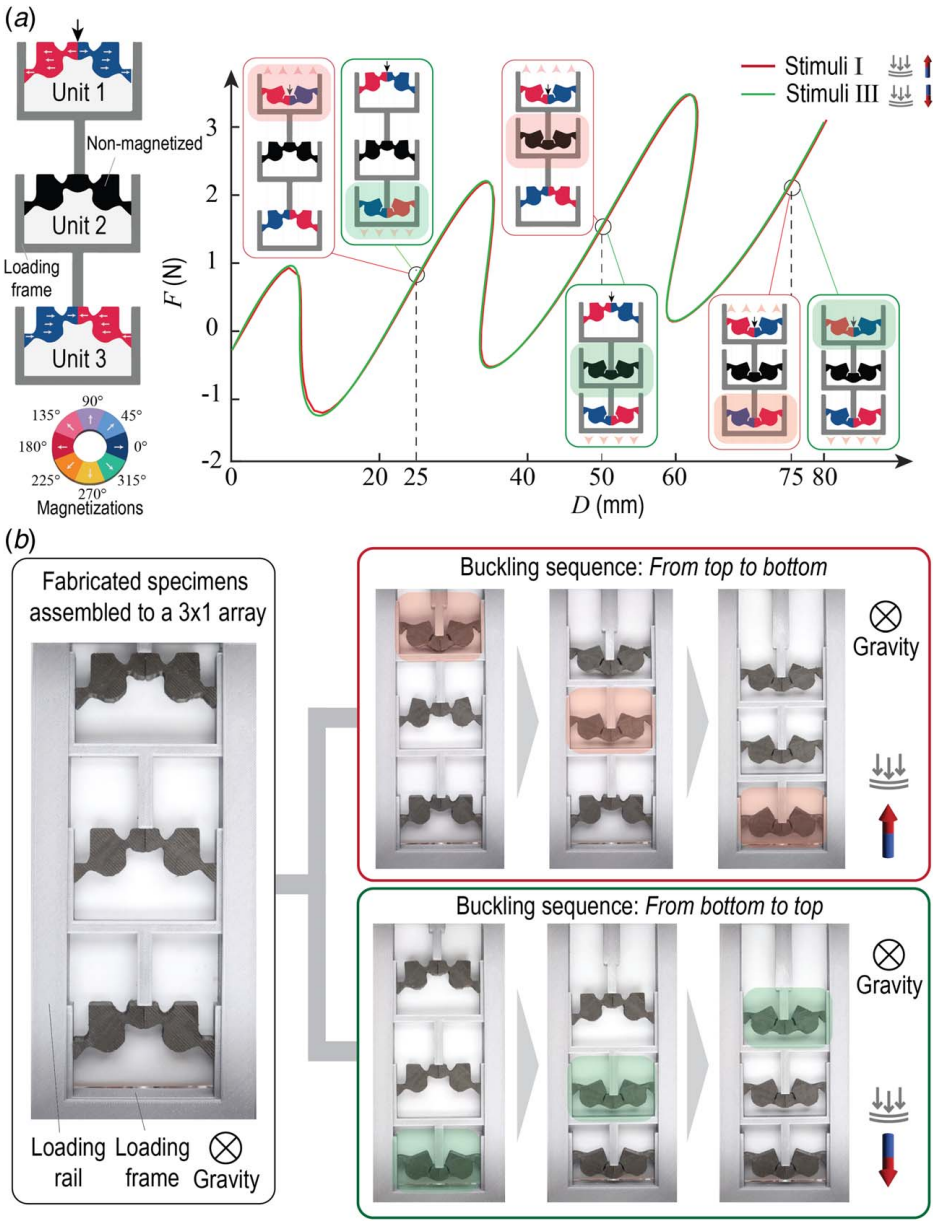

Fig. 8 Programmable sequential buckling enabled by the assembly for the magneto-tunable design with different peak forces: (*a*) assembly setup and force–displacement relations evaluated by FEA and (*b*) experimental demonstration of the sequential buckling behaviors under different magnetic stimuli

altering the peak force levels. We observe that the deformation modes remain unchanged under different stimuli, unlike the actuation mechanism discussed in Sec. 5.1. Interestingly, one of the FD curves (the top curve with stimuli III) does not cross the zero force line, indicating the design's self-recovery property upon release of the mechanical load. For the other two stimuli, we anticipate a self-locking property, meaning a second stable state can be achieved upon the load's release. We conduct five replicates of the experiment and plot the results in Fig. 6(*c*). The experimental results agree well with the numerical simulation, showing consistent peak forces under different stimuli. In contrast to the bonding challenges discussed in Sec. 5.1, the fabrication of this design involves postbonding only the central part, which does not undergo significant deformation. As a result, no bonding failures occur during experimental validation. Supplementary Video 2 compares the loading histories between numerical simulation and experimental validation.

To investigate the controllable self-locking and self-recovery behavior enabled by the magneto-tunable peak force, we conduct an experimental demonstration shown in Fig. 7. A plastic loading frame, rail, and supports are 3D printed to create a gap between the specimen bottom and the ground surface, which reduces friction. To minimize the influence of gravity on the in-plane performance, we horizontally load the specimen and orient gravity out of the plane. Corresponding magnetic fields are applied using a pair of Helmholtz coils for the three sets of stimuli. To compare the self-recovery and self-locking buckling behaviors under different stimuli, the specimen is manually pushed until the members buckled and held in place. The hold is then rapidly released, and the specimen is observed to determine whether it could retain its deformed mode or return to the initial configuration. The results shown in Fig. 7(*b*) indicate that for stimuli I and II, the specimen exhibits self-locking, while for stimulus III, it exhibits self-recovery. This finding is consistent with the expectations obtained from the FD curves in Fig. 6(*c*). Supplementary Video 3 documents the experimental demonstration of magneto-tunable self-locking and self-recovery behaviors.

Additionally, we can utilize the magneto-tunable peak force feature to assemble the design and achieve controlled sequential buckling behaviors. Figure 8(*a*) illustrates a 3×1 assay based on the optimized design, where the three unit structures are connected in parallel through stiff loading frames. To achieve different peak force levels for the three unit structures under a uniform magnetic field pointing upward, we modify the optimized design as follows: Units 1–3 are assigned from top to bottom as the optimized design, the optimized design without pre-magnetization, and the optimized design with reversed magnetization directions, respectively. Unit 1 is the same as the optimized design under stimuli I in Fig. 6. Unit 2 is similar to the design under stimuli II in Fig. 6 since both do not have magnetic actuation. On the basis of our numerical experience, we found that the reversed magnetization distribution under an upward magnetic field can lead to similar magneto-mechanical performance as stimuli III in Fig. 6, which is implemented in unit 3. Using this assembly, the numerical simulation shows that the assembled structure undergoes sequential buckling with the buckling sequence being unit 1, unit 2, and unit 3 under stimuli I (shown in the left box adjacent to each circled point in Fig. 8(*a*)), due to the increased peak force levels for units 1–3. The buckling sequence is reversed (shown in the right box adjacent to each circled point in Fig. 8(*a*)) if we reverse the applied magnetic field, i.e., under stimuli III. To further demonstrate the sequential buckling behavior, we fabricate and test the assembled structure with 3D-printed loading rails and frames. As demonstrated in Fig. 8(*b*), the experimental results show the same sequential buckling behavior under stimuli I and III as predicted by our numerical simulations. Supplementary Video 4 exhibits the experimental demonstration of these two sequential buckling phenomena.

6 Programming Magneto-Induced Buckling Behaviors

This section focuses on the design and analysis of magnetically active structures that exhibit different snap-through buckling behaviors induced by purely magnetic fields. By utilizing the optimization formulation illustrated in Fig. 2(*b*), we obtain two structures that exhibit distinct buckling deformations: self-recovering and self-locking. These structures are then fabricated using a mixture of PDMS and magnetic particles, with a base-to-agent ratio of 25:1 and a magnetic particle volume ratio of 15%. The material properties are characterized following the protocol outlined in the Appendix, and the fabrication procedure is described in detail in Sec. 4.

We perform simultaneous optimization of geometry and magnetization distributions for a clamped rectangular domain with dimensions of 60 mm × 40 mm. We consider a set of $N_m = 8$ candidate magnetization vectors with a uniform orientation space of 45 deg and a constant magnitude of 100 mT. As explained in Sec. 3.4, we indirectly program the snap-through buckling behavior by controlling the FD relations under the mechanical stimuli. We achieve self-locking and self-recovering behaviors by adjusting the force lower bounds so that the FD curve either passes through or avoids the zero force line, respectively. To promote buckling

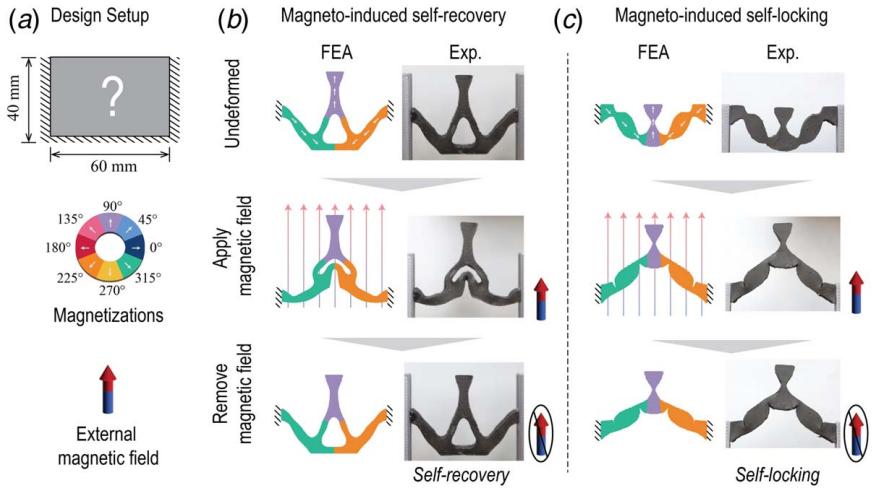

Fig. 9 Numerical and experimental demonstration of magneto-induced buckling structures: (*a*) design setup, (*b*) structure exhibiting self-recovery behavior, and (*c*) structure exhibiting self-locking behavior

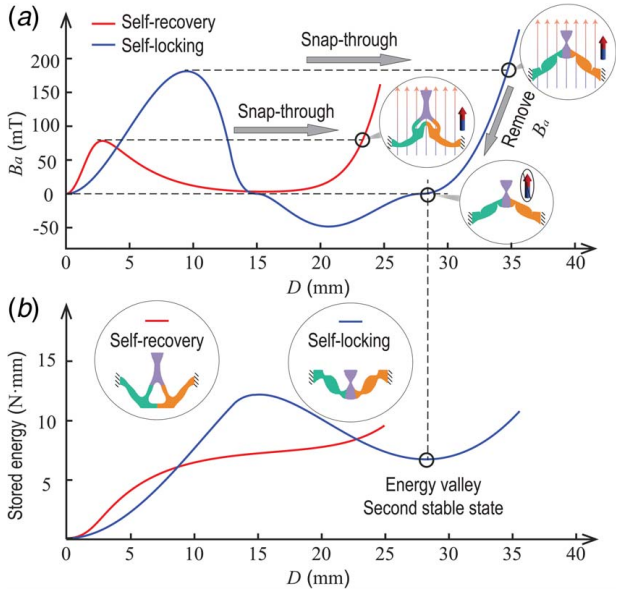

Fig. 10 Two magneto-induced buckling designs with self-locking (right curve with higher maximum B_a value) and self-recovery (left curve with lower maximum B_a value) behaviors: (*a*) B_a–D relations and (*b*) stored energy landscapes

induced by purely magnetic fields, we set displacement constraints to ensure a magneto-actuated displacement greater than $D = 16$ mm. Both structures have a volume fraction of 25%.

The obtained designs are displayed in Fig. 9(*b*). To highlight their distinct self-recovering and self-locking buckling behaviors under the magnetic field, we first apply and then remove a magnetic field (with no mechanical force applied) to observe their deformed configurations. The self-recovering structure exhibits upward deformation under the magnetic field, with the left and right members undergoing buckling. Upon removal of the magnetic field, the structure reverts to its original undeformed configuration. Instead, the self-locking structure, which can also deform upward and buckle under the applied magnetic field, retains its deformed state after the magnetic field is removed, exhibiting a second stable state. In our experimental demonstration, we use permanent magnets to actuate the two corresponding fabricated specimens[2] and verify that the structures display the expected self-recovering and self-locking buckling behaviors under magnetic actuation, which agrees well with our numerical findings. Supplementary Video 5 documents the experimental demonstration of magneto-induced self-locking and self-recovery behaviors.

In order to investigate the origins of the distinct buckling behavior exhibited by the two designs, we perform simulations of the B_a–D (magnitude of external magnetic flux density versus displacement) responses and the energy landscapes associated with the two structures. The displacement is evaluated at the middle top of the designs. The curves shown in Fig. 10 are obtained through the arc-length method [42]. We note that the stored energy is computed by summing up the elementwise stored energy (excluding magnetic energy because it is an external stimulus) on the body-fitted mesh for the optimized design. Our simulations indicate that the B_a-D curve of the self-recovering structure does not go below the 0–B_a line, indicating no second energy valley in the stored energy landscape. Conversely, the self-locking design exhibits a B_a–D curve going below the 0–B_a line, and its corresponding stored energy landscape exhibits a second stable state. These findings suggest that the self-locking design has bistability and is capable of self-locking upon the application and removal of the external magnetic field.

[2]We employ permanent magnets in this demonstration.

7 Conclusion Remarks

This study presents a tailored magneto-mechanical topology optimization framework and experimental validation to precisely program various buckling behaviors into magnetically active structures. By leveraging magneto-mechanical interactions, our framework enables the systematic design of structures with programmable buckling responses under either magneto-mechanical or purely magnetic stimuli. The optimized designs demonstrate a range of tunable buckling behaviors, including controllable mechano-induced responses with varying levels of displacement, peak force, and bistability, as well as magneto-induced responses with self-recovering or self-locking deformations.

We reveal that the key mechanisms driving the tunable buckling responses in these structures are the magnetic torque-induced bending deformations of member joints under distinct applied magnetic fields. Furthermore, by assembling multiple optimized designs into architectures, we create architected materials with tunable multistability and programmable buckling sequences under varying magnetic fields. By utilizing a hybrid fabrication technique, we manufacture these optimized designs and validate their programed magneto-mechanical buckling behaviors by comparing experimental results with numerical simulations. The excellent agreement between numerical predictions and experimental findings across all cases validates the effectiveness of our proposed inverse design framework. The proposed framework provides a systematic paradigm for realizing multifunctional materials and structures with programmable and tunable nonlinear responses, opening up new possibilities for their applications in robotics, energy absorption, actuation, and assembly mechanisms.

For future work, we plan to employ topology optimization to design energy harvesting devices that harness magneto-induced buckling to create large magnetoelectricity [44,45]. Another important future direction of research is to analyze the stability and bifurcation of the resulting magnetic systems analytically [46] to provide a more comprehensive understanding of the behaviors of such systems.

Acknowledgment

The authors acknowledge the financial support from the U.S. Defense Advanced Research Projects Agency (DARPA) Young Faculty Award (N660012314013) and the U.S. National Science Foundation (NSF) CAREER Award CMMI-2047692. The information provided in this paper is the sole opinion of the authors and does not necessarily reflect the view of the sponsoring agency. The authors acknowledge the use of facilities and instrumentation at the Materials Research Laboratory Central Research Facilities, University of Illinois, partially supported by NSF through the University of Illinois Materials Research Science and Engineering Center DMR-1720633.

Conflict of Interest

There are no conflicts of interest.

Data Availability Statement

The datasets generated and supporting the findings of this article are obtainable from the corresponding author upon reasonable request.

Appendix: Material Characterization

The mechanical properties of the material are characterized by fitting the parameters in the constitutive model (Eqs. (2) and (3)) to the stress–strain relationships obtained from testing dog-bone specimens according to standard [47] in tension, and cylinder

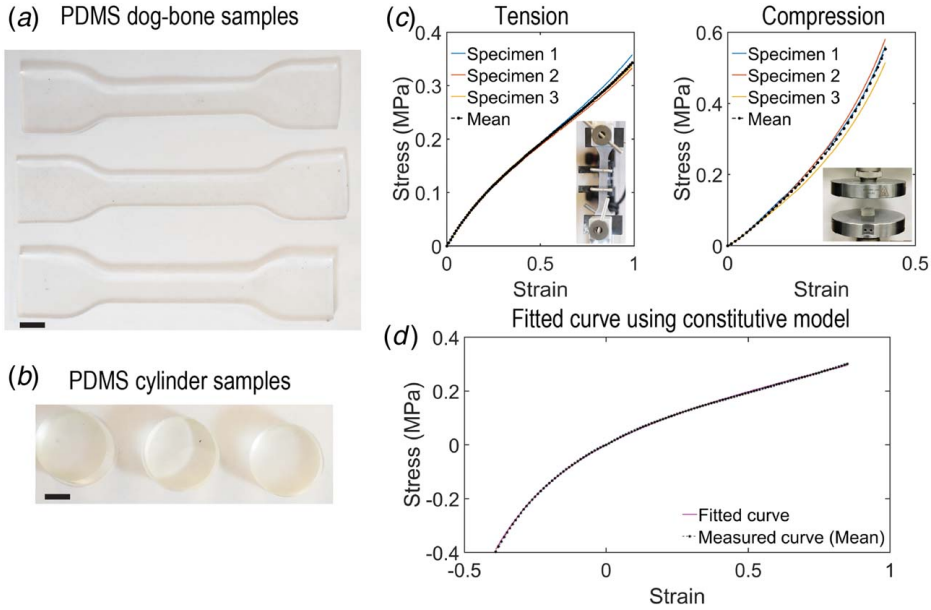

Fig. 11 Characterization of PDMS material with a base-to-agent ratio of 20:1: (*a*) tension samples (scale bar 10 mm), (*b*) compression samples (scale bar 10 mm), (c) testing data, and (*d*) fitted curve using the constitutive model

specimens according to standard [48] in compression. The measured volume ratio of magnetic particles (15%) is also necessary to be input into the model. The designs described in Sec. 5 are produced using PDMS with a base-to-agent ratio of 20:1, and the corresponding characterization data are presented in Fig. 11. For the designs described in Sec. 6, PDMS with a base-to-agent ratio of 25:1 is used. In terms of magnetic properties, the PDMS with magnetic particles at a volume ratio of 15% is measured to have a residual magnetic flux density of 100 mT using a vibrating-sample magnetometer (Quantum Design MPMS3).

References

[1] Chi, Y., Li, Y., Zhao, Y., Hong, Y., Tang, Y., and Yin, J., 2022, "Bistable and Multistable Actuators for Soft Robots: Structures, Materials, and Functionalities," Adv. Mater., **34**(19), p. 2110384.

[2] Hu, N., and Burgueño, R., 2015, "Buckling-Induced Smart Applications: Recent Advances and Trends," Smart Mater. Struct., **24**(6), p. 063001.

[3] Tan, X., Wang, B., Yao, Y., Yao, K., Kang, Y., Zhu, S., Chen, S., and Xu, P., 2020, "Programmable Buckling-Based Negative Stiffness Metamaterial," Mater. Lett., **262**, p. 127072.

[4] Xu, Z., Fan, Z., Zi, Y., Zhang, Y., and Huang, Y., 2020, "An Inverse Design Method of Buckling-Guided Assembly for Ribbon-Type 3d Structures," ASME J. Appl. Mech., **87**(3), p. 031004.

[5] Hua, J., Lei, H., Gao, C.-F., and Fang, D., 2022, "A Novel Design of Multistable Metastructure With Nonuniform Cross Section," ASME J. Appl. Mech., **89**(5), p. 051010.

[6] Li, Z., and Saif, M. T. A., 2021, "Mechanics of Biohybrid Valveless Pump-Bot," ASME J. Appl. Mech., **88**(11), p. 111004.

[7] Alturki, M., and Burgueño, R., 2019, "Multistable Cosine-Curved Dome System for Elastic Energy Dissipation," ASME J. Appl. Mech., **86**(9), p. 091002.

[8] Cleary, J., and Su, H.-J., 2015, "Modeling and Experimental Validation of Actuating a Bistable Buckled Beam Via Moment Input," ASME J. Appl. Mech., **82**(5), p. 051005.

[9] Li, H., Wang, X., Zhu, F., Ning, X., Wang, H., Rogers, J. A., Zhang, Y., and Huang, Y., 2018, "Viscoelastic Characteristics of Mechanically Assembled Three-Dimensional Structures Formed by Compressive Buckling," ASME J. Appl. Mech., **85**(12), p. 121002.

[10] Kim, Y., and Zhao, X., 2022, "Magnetic Soft Materials and Robots," Chem. Rev., **122**(5), pp. 5317–5364.

[11] Zhao, R., Kim, Y., Chester, S. A., Sharma, P., and Zhao, X., 2019, "Mechanics of Hard-Magnetic Soft Materials," J. Mech. Phys. Solids., **124**, pp. 244–263.

[12] Zhang, R., Wu, S., Ze, Q., and Zhao, R., 2020, "Micromechanics Study on Actuation Efficiency of Hard-Magnetic Soft Active Materials," ASME J. Appl. Mech., **87**(9), p. 091008.

[13] Chen, T., Pauly, M., and Reis, P. M., 2021, "A Reprogrammable Mechanical Metamaterial With Stable Memory," Nature, **589**(7842), pp. 386–390.

[14] Abbasi, A., Sano, T. G., Yan, D., and Reis, P. M., 2023, "Snap Buckling of Bistable Beams Under Combined Mechanical and Magnetic Loading," Philos. Trans. R. Soc. A, **381**(2244), p. 20220029.

[15] Yan, D., Pezzulla, M., Cruveiller, L., Abbasi, A., and Reis, P. M., 2021, "Magneto-Active Elastic Shells With Tunable Buckling Strength," Nat. Commun., **12**(1), p. 2831.

[16] Pal, A., and Sitti, M., 2023, "Programmable Mechanical Devices Through Magnetically Tunable Bistable Elements," Proc. Natl. Acad. Sci. USA, **120**(15), p. e2212489120.

[17] Bendsoe, M. P., and Sigmund, O., 2013, *Topology Optimization: Theory, Methods, and Applications*, Springer Science & Business Media, Heidelberg, Germany.

[18] Wang, C., Zhao, Z., Zhou, M., Sigmund, O., and Zhang, X. S., 2021, "A Comprehensive Review of Educational Articles on Structural and Multidisciplinary Optimization," Struct. Multidiscipl. Optim., **64**, pp. 1–54.

[19] Bruns, T., Sigmund, O., and Tortorelli, D. A., 2002, "Numerical Methods for the Topology Optimization of Structures that Exhibit Snap-through," Int. J. Numer. Methods Eng., **55**(10), pp. 1215–1237.

[20] Bhattacharyya, A., Conlan-Smith, C., and James, K. A., 2019, "Design of a Bi-stable Airfoil With Tailored Snap-Through Response Using Topology Optimization," Comput. Aided Des., **108**, pp. 42–55.

[21] Li, W., Wang, F., Sigmund, O., and Zhang, X. S., 2022, "Digital Synthesis of Free-Form Multimaterial Structures for Realization of Arbitrary Programmed Mechanical Responses," Proc. Natl. Acad. Sci. USA, **119**(10), p. e2120563119.

[22] Zhao, Z., and Zhang, X. S., 2022, "Topology Optimization of Hard-Magnetic Soft Materials," J. Mech. Phys. Solids, **158**, p. 104628.

[23] Tian, J., Li, M., Han, Z., Chen, Y., Gu, X. D., Ge, Q., and Chen, S., 2022, "Conformal Topology Optimization of Multi-Material Ferromagnetic Soft Active Structures Using an Extended Level Set Method," Comput. Methods. Appl. Mech. Eng., **389**, p. 114394.

[24] Zhao, Z., and Zhang, X. S., 2023, "Encoding Reprogrammable Properties Into Magneto-Mechanical Materials Via Topology Optimization," NPJ Comput. Mater., **9**(1), p. 57.

[25] Wang, C., Zhao, Z., and Zhang, X. S., 2023, "Inverse Design of Magneto-Active Metasurfaces and Robots: Theory, Computation, and Experimental Validation," Comput. Methods. Appl. Mech. Eng. In Press.

[26] Yan, D., Aymon, B. F., and Reis, P. M., 2023, "A Reduced-Order, Rotation-Based Model for Thin Hard-Magnetic Plates," J. Mech. Phys. Solids., **170**, p. 105095.

[27] Mukherjee, D., Rambausek, M., and Danas, K., 2021, "An Explicit Dissipative Model for Isotropic Hard Magnetorheological Elastomers," J. Mech. Phys. Solids., **151**, p. 104361.

[28] Leonard, M., Wang, N., Lopez-Pamies, O., and Nakamura, T., 2020, "The Nonlinear Elastic Response of Filled Elastomers: Experiments vs. Theory for the Basic Case of Particulate Fillers of Micrometer Size," J. Mech. Phys. Solids., **135**, p. 103781.

[29] Lopez-Pamies, O., 2010, "A New I1-Based Hyperelastic Model for Rubber Elastic Materials," Comptes Rendus Mecanique, **338**(1), pp. 3–11.

[30] Belytschko, T., Liu, W. K., Moran, B., and Elkhodary, K., 2014, *Nonlinear Finite Elements for Continua and Structures*, John Wiley & Sons, Chichester, UK.

[31] Armijo, L., 1966, "Minimization of Functions Having Lipschitz Continuous First Partial Derivatives," Pac. J. Math., **16**(1), pp. 1–3.
[32] Zhang, X., Ramos, A. S., and Paulino, G. H., 2017, "Material Nonlinear Topology Optimization Using the Ground Structure Method With a Discrete Filtering Scheme," Struct. Multidiscipl. Optim., **55**(6), pp. 2045–2072.
[33] Wang, F., Lazarov, B. S., and Sigmund, O., 2011, "On Projection Methods, Convergence and Robust Formulations in Topology Optimization," Struct. Multidiscipl. Optim., **43**(6), pp. 767–784.
[34] Bourdin, B., 2001, "Filters in Topology Optimization," Int. J. Numer. Methods Eng., **50**(9), pp. 2143–2158.
[35] Bendsøe, M. P., 1989, "Optimal Shape Design as a Material Distribution Problem," Struct. Optim., **1**(4), pp. 193–202.
[36] Zhou, Y., Nomura, T., and Saitou, K., 2018, "Multi-Component Topology and Material Orientation Design of Composite Structures (MTO-C)," Comput. Methods. Appl. Mech. Eng., **342**, pp. 438–457.
[37] Wang, F., Lazarov, B. S., Sigmund, O., and Jensen, J. S., 2014, "Interpolation Scheme for Fictitious Domain Techniques and Topology Optimization of Finite Strain Elastic Problems," Comput. Methods. Appl. Mech. Eng., **276**, pp. 453–472.
[38] Deng, H., Cheng, L., Liang, X., Hayduke, D., and To, A. C., 2020, "Topology Optimization for Energy Dissipation Design of Lattice Structures Through Snap-Through Behavior," Comput. Methods Appl. Mech. Eng., **358**, p. 112641.
[39] Duysinx, P., and Bendsøe, M. P., 1998, "Topology Optimization of Continuum Structures With Local Stress Constraints," Int. J. Numer. Methods Eng., **43**(8), pp. 1453–1478.
[40] Bruggi, M., 2008, "On an Alternative Approach to Stress Constraints Relaxation in Topology Optimization," Struct. Multidiscipl. Optim., **36**(2), pp. 125–141.
[41] Svanberg, K., 1987, "The Method of Moving Asymptotes—A New Method for Structural Optimization," Int. J. Numer. Methods Eng., **24**(2), pp. 359–373.
[42] Leon, S. E., Lages, E. N., De Araújo, C. N., and Paulino, G. H., 2014, "On the Effect of Constraint Parameters on the Generalized Displacement Control Method," Mech. Res. Commun., **56**, pp. 123–129.
[43] Kim, Y., Yuk, H., Zhao, R., Chester, S. A., and Zhao, X., 2018, "Printing Ferromagnetic Domains for Untethered Fast-Transforming Soft Materials," Nature, **558**(7709), pp. 274–279.
[44] Rahmati, A. H., Jia, R., Tan, K., Zhao, X., Deng, Q., Liu, L., and Sharma, P., 2023, "Theory of Hard Magnetic Soft Materials to Create Magnetoelectricity," J. Mech. Phys. Solids., **171**, p. 105136.
[45] Rahmati, A. H., Jia, R., Tan, K., Liu, L., Zhao, X., Deng, Q., and Sharma, P., 2023, "Giant Magnetoelectricity in Soft Materials Using Hard Magnetic Soft Materials," Mater. Today Phys., **31**, p. 100969.
[46] Yang, S., and Sharma, P., 2023, "A Tutorial on the Stability and Bifurcation Analysis of the Electromechanical Behaviour of Soft Materials," Appl. Mech. Rev., **75**(4), pp. 044801.
[47] ASTM-D412, 2016, Standard Test Methods for Vulcanized Rubber and Thermoplastic Elastomers—Tension. ASTM International, West Conshohocken, PA.
[48] ASTM-D575, 2018, Standard Test Methods for Rubber Properties in Compression, ASTM International, West Conshohocken, PA.